Unique corrosion behavior of an archaeological Roman iron ring: Microchemical characterization and thermodynamic considerations

Valentina Valbi, Fabio Enrico Furcas, Delphine Neff, Philippe Dillmann, Ueli Angst, Myriam Krieg, Anika Duvauchelle, Marion Berranger, Stefano Mischler, Laura Brambilla, et al.

Unique corrosion behavior of an archaeological Roman iron ring: microchemical characterization and thermodynamic considerations.

Valentina Valbi[1], Fabio Enrico Furcas[2], Delphine Neff[3], Philippe Dillmann[3], Ueli Angst[2], Myriam Krieg[4], Anika Duvauchelle[4], Marion Berranger[1], Stefano Mischler[5], Laura Brambilla[6], Naima Gutknecht[6], Christian Degrigny[6]

[1]Laboratoire Métallurgies et Cultures (LMC-IRAMAT-UMR7065-CNRS), Université Technologique de Belfort-Montbéliard, Belfort, France

[2]Institute for Building Materials, ETH Zürich, Laura-Hezner-Weg 7, 8093, Zürich, Switzerland

[3]Laboratoire Archéomatériaux et Prévision de l'Altération (LAPA), IRAMAT/NIMBE CEA, CNRS, Université Paris-Saclay, CEA Paris-Saclay, Gif-sur-Yvette, France

[4]Site et Musée romains d'Avenches (SMRA), Avenches, Switzerland

[5]Tribology and Interfacial Chemistry (TIC), EPFL, Lausanne, Switzerland

[6]Haute Ecole Arc Conservation-restauration / HES-SO, Neuchâtel, Switzerland

Corresponding author: valentinavalbi@gmail.com

Abstract

The corrosion mechanisms of a Roman iron bezel ring were investigated by in-depth characterization of its uncommon corrosion pattern and thermodynamic modelling. A silver foil and altered glass remnants were identified, covered with thick strata of magnetite and goethite. Underneath it, was a multi-millimetric cavity, filled with spheroidal magnetite or magnetite/goethite nodules in a siderite matrix. The bottom of the preserved object showed a marbled corrosion structure composed of goethite, magnetite/maghemite and hematite. Heterogeneous and evolving local conditions, involving synergistic effects of electrolytic and dissolution/precipitation mechanisms might explain the unique morphology and nature of the corrosion products observed.

Keywords

Iron (A), Silver (A), SEM (B), Raman spectroscopy (B), Interfaces (C), oxidation (C)

1. Introduction

Historical and archaeological metallic artefacts are exposed to corrosive environments, both in their original and/or museal locations. These environments could be different types of archaeological soils and underwater sites, or atmospheric media (also in storage deposits, and museum exhibition rooms

when atmospheric conditions are not sufficiently controlled). All these varying environmental conditions can even cause severe material degradations. A thorough diagnostic is necessary to preserve these objects and apply appropriate conservation treatments [1,2]. Due to the possible complexity of the corrosion patterns, a combination of non-invasive and invasive characterization techniques is needed to elucidate the long-term corrosion mechanisms. Thus, in the frame of the MetalPAT project, the conservation state of ancient metallic artefacts was assessed in order to implement the MiCorr database (micorr.org) of corrosion forms, presented as corrosion product stratigraphies [3]. Among these artefacts, the iron ring from Avenches (inv. 16/17330-02), corroded in an archaeological soil and presenting an advanced stage of degradation with an uncommon corrosion pattern [4], provided a unique opportunity to study a peculiar and atypical corrosion phenomenon.

The generalized corrosion of archaeological iron artefacts in soil has been widely described in the literature [5–10]. Several factors can influence the corrosion mechanisms; intrinsic parameters such as the type of metal or alloy and its microstructure, and environmental parameters such as pH, oxidation/reduction potential, conductivity and aeration of the soil [11,12]. Aerated oxidizing conditions favor the formation of oxyhydroxides including goethite (α-FeOOH), while more reducing conditions favor the formation of carbonates such as siderite ($FeCO_3$) [6,13–17]. Selected chloride-induced corrosion scenarios [18], or the presence of sulphides in the corrosion system [19,20] have also been investigated. Thus, the nature, morphology and distribution of corrosion products on or in the vicinity of the corroding artefact are direct indicators of specific corrosion conditions. Besides, the identification of the original surface, and thus the original shape of the object, is particularly important in conservation science for an appropriate conservation-restoration treatment of the artefact [6,21], but also for the understanding of the object in archaeological science. Since historical and stylistic considerations are based on topological and morphological observations of the object shape and surface, a deformation of the surface could thus lead to a misinterpretation of the artefact if not well recognized as the result of a corrosion phenomenon.

In soils, the most common corrosion stratigraphy is usually composed of the residual metal (M), of a dense product layer (DPL) composed of compact well-crystallized corrosion products, and a transformed medium (TM) consisting in a mixture of corrosion products with external markers, in contact with the soil (S) [6]. The original surface of the object is generally assumed to correspond to the interface between the DPL and the TM. Nevertheless, the work by Krieg et al. [4] on the iron ring from Avenches showed that this object did not present the classical corrosion structure like the one described in the literature for archaeological iron objects corroded in soil. The ring was recovered in the excavation of the Roman site of Avenches in the *extra muros* sector *Sur Fourches,* inhabited between the middle of the 2nd century BC and the Roman period. At the intersection of the alluvial cones of two small streams, the sector was characterized by very active groundwater circulation and the level of the shallow water table was sensitive to significant fluctuations on rainfall. When it was discovered, the object was found

completely covered by a thick layer of sediment and corrosion products. Based on micro-sandblasting and non-invasive analysis performed by Krieg et al. [4], the ring was tentatively classified as part of the category of Roman bezel ring Type 2a (see Figure 1a for a schematic drawing of the supposed original state of the ring). This type of bezel ring is always decorated with an inlay (stone, glass paste, enamel or metal inlay imitating an intaglio), which means that the base of the bezel is always flat [22]. In their preliminary non-invasive investigation including X-Ray µ-tomography and surface characterization by SEM-EDX and µ-Raman spectroscopy, Krieg et al. [4] indeed identified a silver foil underneath an external layer of corrosion products (goethite and magnetite), but no other form of embellishment was detected. The µ-tomography images also evidenced the presence of a convex cavity in the center of the ring, partially filled with unidentified corrosion products. This peculiar morphology of the corroded object (see Figure 1b for the picture of the artefact at the time of investigation), distinctly different from the assumed ring's original flat appearance.

Taking advantage of the rare opportunity to perform invasive investigation on such a unique artefact, the present work aims to complete the characterization of the Roman ring by a micrometric and sub-micrometric mapping of corrosion products on a transverse section. Insights into the distribution of iron corrosion products further assist the interpretation of the degradation mechanisms also based on some thermodynamic consideration.

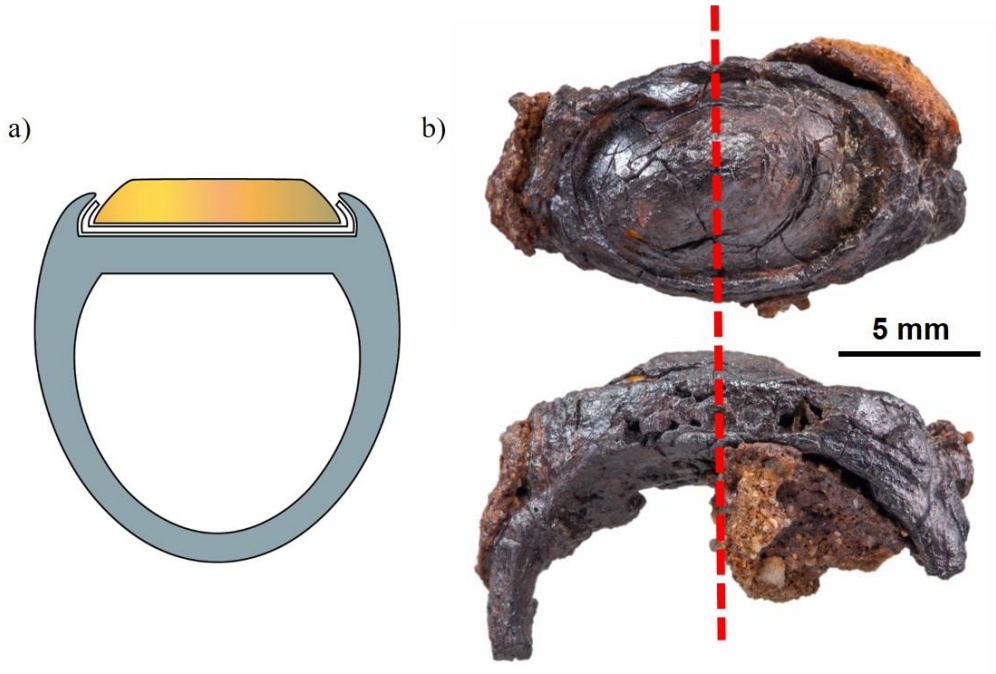

Figure 1 The Roman iron ring from Avenches. a) Schematic drawing of an uncorroded Roman Type 2a bezel ring, b) Photographic documentation of the corroded object with detail of the cutting area (dotted red line) for observation on transverse section. Modified with permission from Krieg et al.[4].

2. Methods

The object was entirely embedded in resin (Struers SpeciFix 40) and cross-sectioned with a micro rotatory tool (Figure 1b). The object was cut at the center, in the same direction as the tomographic views obtained by Krieg et al. [4]. The cross-section of the sample was then ground with silicon carbide paper (grade 80, 180, 300, 800, and 1200) and a final polish was done with diamond paste (6, 3, and 1 µm) using ethanol as wetting agent. The cross section was observed on a numerical optical microscope KEYENCE VHX-7000 in bright field mode.

Chemical investigation of major elements (i.e. elements weight > 0.5%) was achieved using Energy Dispersive X-ray Spectrometry (EDX with silicon drift detector (SDD) large window allowing counting rates about 90 000 c/s) coupled to a Scanning Electron Microscope (SEM-FEG JEOL 7001-F). Prior to SEM-EDX observations, the sample was coated with a carbon layer. EDX analyses were performed at a working distance (WD) of 10 mm, with an accelerating voltage of 15 kV and probe current of ~9 nA. For each spectrum, background contribution was automatically removed using a digital top hat filter. Then quantification was done using XPP correction routine with inner standards (matrix correction with Phi-Rho-Z). The relative error for elemental quantification was considered to be 10% for content range <1wt.%, and 2% for content range >1wt.%. Detailed morphological observations of the corrosion products were obtained in secondary electron mode with a lower WD (3.6-3.7 mm).

µ-Raman spectroscopy was performed on a HORIBA Labram Xplora spectrometer equipped with a 532 nm and a 785 nm laser with a 1800 gr/mm groove density grating. The laser power employed for the identification of the iron corrosion products was between 0.04 and 0.55 mW for the 532 nm laser and between 0.1 and 0.7 mW for the 785 nm laser, in order to avoid heat-transformation of the phases under the beam. When not specified, the 532 nm laser was employed. Measurements were realized under a microscope with a x100 objective. Spatial resolution was around 2 µm and spectral resolution about 2 cm^{-1}. Acquisition time varied between 1 and 5 minutes. Mineralogical phases were compared with reference spectra [5,6,23] of the most common iron corrosion products (goethite, lepidocrocite**,** siderite, magnetite, maghemite, hematite), a summary of the main peaks used for the identification of the corrosion products encountered in this work are reported in Table 1.

Table 1 Raman main peaks used for the identification of the corrosion products.

Corrosion product	**Raman main peaks (cm^{-1})**	**Reference**
Goethite (α-FeOOH)	245, 301, **388**, 482, 550, 685	Neff et al., 2004
Magnetite (Fe_3O_4)	308, 542, **669**	Neff et al., 2004
Maghemite (γ-Fe_2O_3)	380, 510, **670, 720**	Neff et al., 2005
Hematite (α-Fe_2O_3)	**228**, 296, 415, 510, 672, 1333	Neff et al., 2004
Siderite ($FeCO_3$)	285, 729, **1084**	RRUFF database Lafuente et al., 2015

The GEM-Selektor (GEMS3K) thermodynamic modelling framework was used to compute the composition-dependent stability of various characterized solid iron (hydr)oxide phases [24,25]. The activity coefficient of aqueous species *i* was calculated with the extended Debye-Hückel equation in Truesdell-Jones form:

$$\log_{10}\gamma_i = \frac{A\cdot[z_i]^2\cdot\sqrt{I}}{1+B\cdot a\sqrt{I}} + b_\gamma \cdot I + \log_{10}\frac{x_{i,w}}{X_w}, \qquad (1)$$

where b_γ is an electrolyte-specific semi-empirical parameter ($b_\gamma \sim$ 0.064 for NaCl), z_i is the formal charge of species *i*, $x_{i,w}/x_w$ is the mole fraction of water and A ~ 0.5114 and B ~ 0.3288 are the Debye-Hückel Limiting Law parameters evaluated at T = 25 °C and pressure P = 1 bar [24,26]. Equation (1) is applicable to ionic strengths *I* of up to 2 mol/L. All simulations employed state-of-the art thermodynamic parameters of iron (hydr)oxides and aqueous complexes [27,28] as well as the standard molar Gibbs free energies ($\Delta_f G_m^\circ$) and enthalpies ($\Delta_f H_m^\circ$) of formation and entropies (S_m°) of a range of auxiliary species including NaCl, O_2(g) and H_2(g) [29]. For a more detailed account of the calculation methodology and a compilation of thermodynamic parameters, the reader is referred to Furcas et al. [28].

3. **Results**

Optical microscopy (OM) observation in bright field mode of the whole cross-section of the sample (Figure 2) revealed a heterogeneous structure. Only a very small residual metallic iron fragment was observed (just a few micrometers) in the left extremity of Figure 2 (black arrow). The uncorroded silver foil (white arrow in Fig.2) was detected as well in the upper part of the object. Dense corrosion products were observed in the external parts of the sample, while the center of the object presented a large cavity partially filled with nodular corrosion products. Three Regions of Interest (ROI), corresponding to the top (ROI1), the bottom (ROI2), and the center (ROI3) of the ring were chosen to detail the nature and morphology of the identified compounds. They are reported in Figure 2 (ROI1: blue, ROI2: green, ROI3: yellow), they will be further described in the following paragraphs. If not specified, the colors used to describe the different corrosion products refer to the colors observed under optical microscopy in bright field mode. Also, when spatial indicators such as right, left, upper/top, bottom, are used to indicate a certain area of the sample, they refer to the configuration of the sample as depicted in Figure 2, and do not in any way reflect its position in the soil.

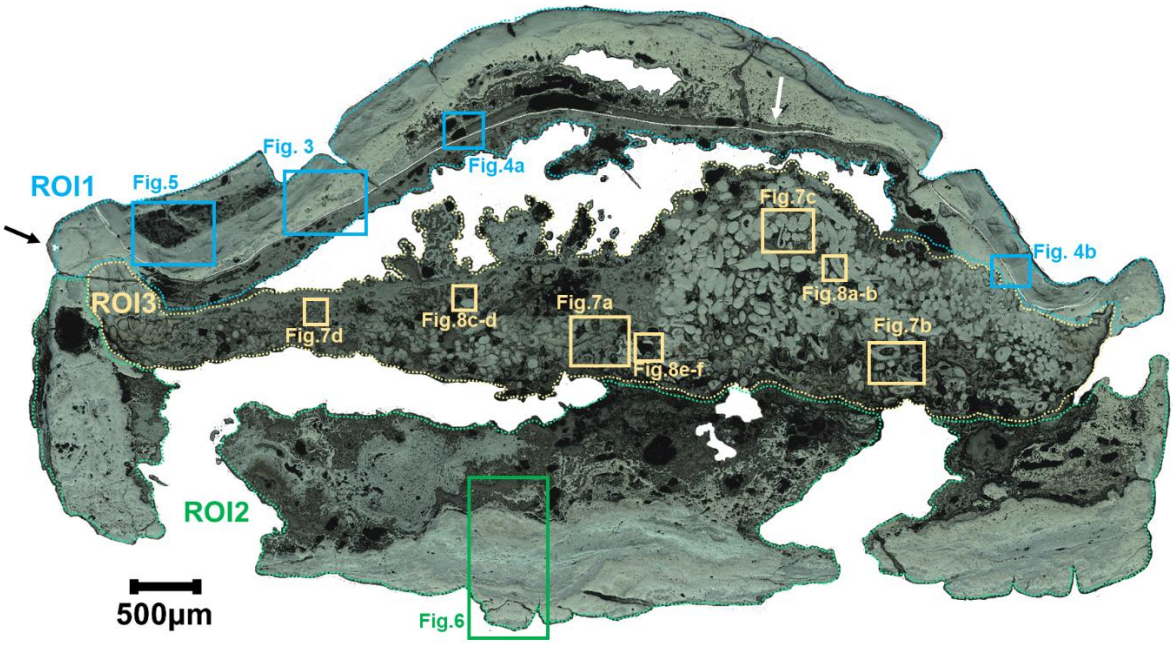

Figure 2 Optical microscopy image of the sample in cross-section, with identification of different regions of interest (color-coded) and localization of the following figures. Region of interest 1 - ROI1 (blue) corresponds to the top of the sample around the silver foil (indicated by a white arrow), detailed in Figs.3-4-5. Region of interest 2 – ROI2 (green) corresponds to the bottom of the sample with a marbled corrosion structure, detailed in Fig.6. Region of interest 3- ROI3 (yellow) corresponds to the central area of the sample with nodular corrosion products, detailed in Figs.7-8. Residual metallic iron is indicated by a black arrow.

3.1 Region of Interest 1: top area/upper part of the ring

The area in Figure 3 is located in ROI1 in the upper external part of the sample. First, a thin and well-defined bright layer with a homogenous thickness of 4 ± 1 µm (mean value and standard deviation from 15 measurements at different locations in the sample) is visible on the OM (Fig. 3a) and SEM (Fig. 3b-e) images. This layer corresponded to a metal foil composed of 98 wt.% Ag and 2 wt.% Cu, as determined by EDX (Fig. 3e), trapped in Fe- and O-rich corrosion products (Fig. 3c and Fig. 3d). Starting from the external part of the sample (upper part in Figure 3), it was possible to observe in Fig. 3a and Fig. 3b an approximately 200 µm thick layer of corrosion products composed of a predominant phase appearing grey in both OM and SEM images, with light grey thin bands within it (from a minimum of 2-3 µm to a maximum of 90 µm thick). For the grey phase, 64 wt.% of Fe and 33 wt.% of O were detected by SEM-EDX, while the Raman spectrum (point R28 in Fig. 3a and corresponding spectrum in Fig. 3f) showed peaks at 301, 388, 482, 550 and 685 cm^{-1}, allowing the identification of the iron oxyhydroxide goethite (α-FeOOH). The thin bands of light grey corrosion products within this grey goethite layer showed a Raman spectrum (point R27 in Fig. 3a) with a main broad band around 700 cm^{-1} with two shoulders at 660 and 720 cm^{-1} (Fig. 3g) corresponding to a mixture of the magnetite (α-Fe_3O_4) and maghemite (γ-Fe_2O_3) oxides. Below this external zone, a light grey layer (100-200 µm thick) with small grey islets (5 to 50 µm thick) was observed in contact with the silver foil in Fig. 3a and Fig. 3b. For the light grey phase, 74 wt.% of Fe and 36 wt.% of O were detected by SEM-EDX, while the Raman

spectrum (point R20 in Fig. 3a) showed peaks at 308, 542 and 669 cm^{-1} (Fig. 3h), allowing the identification of magnetite. The small grey islets within the thick magnetite layer were identified as goethite (Raman point 21 in Fig. 3a and corresponding spectrum in Fig. 3f). Underneath the silver foil, a 100-120 µm thick dark grey layer was observed in Fig. 3a and Fig. 3b, showing a Raman spectrum (point R24 in Fig. 3a) with peaks at 285, 729, 1084 cm^{-1} (Fig. 3i) and identified the phase as siderite ($FeCO_3$). Underneath the siderite layer, a discontinuous thin layer (20-30 µm thick) of grey and light grey corrosion products, identified respectively as goethite (point R26 in Fig. 3a and corresponding spectrum in Fig. 3f) and magnetite (point 25 in Fig. 3a and corresponding spectrum in Fig.3h), was observed next to the central cavity.

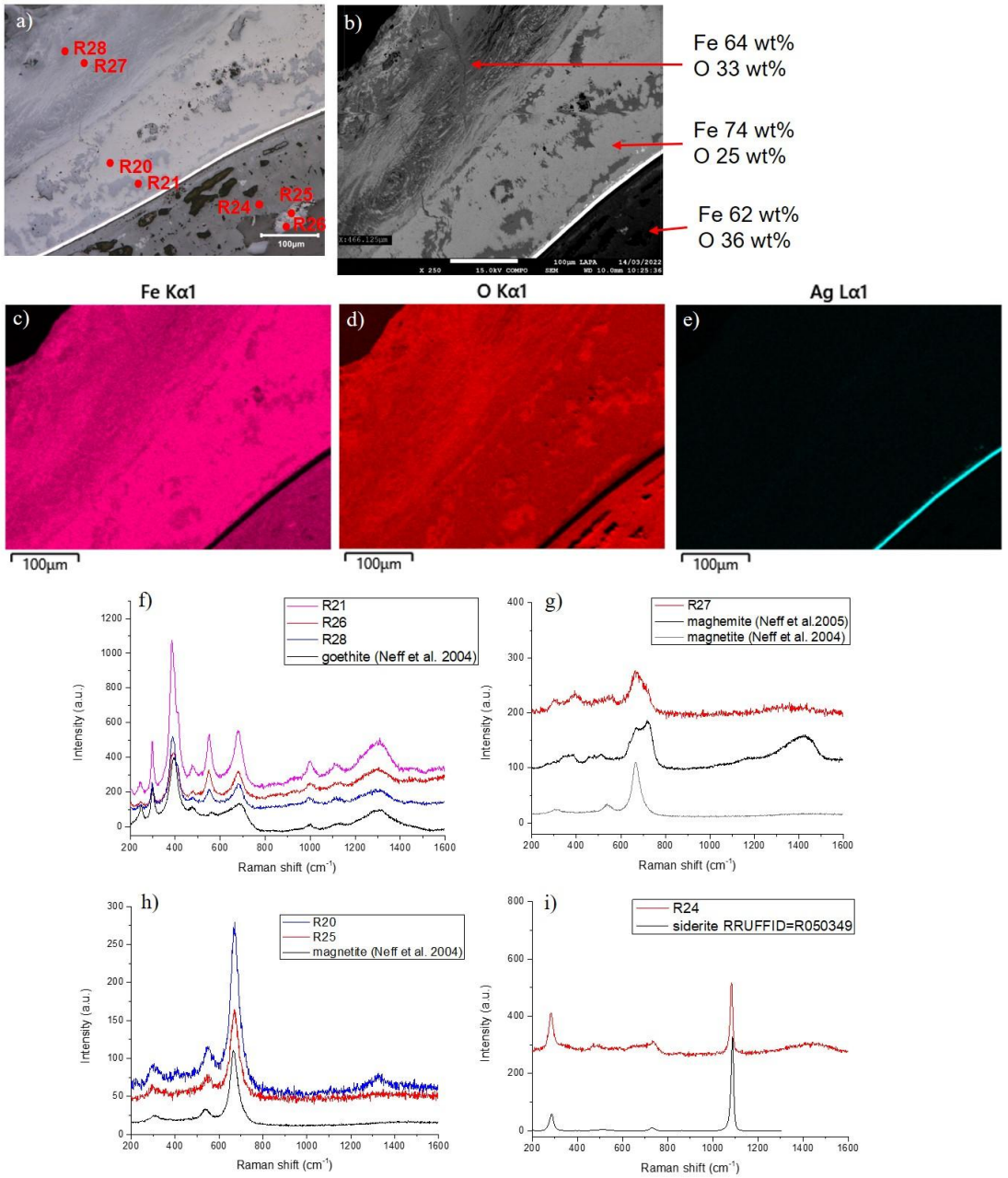

Figure 3 a) Optical microscopy image (with identification of the µ-Raman analysis points) of an area in ROI1, the upper part of the sample as depicted in Figure 2. b) Backscattered electron image with

EDX composition of the different corrosion products and EDX elemental mapping for c) Fe, d) O and e) Ag. µ-Raman spectra for f) R21, R26 and R28 analysis points, g) R27 analysis point, h) R20 and R25 analysis points, i) R24 analysis point.

On several locations throughout ROI1, fracture points of the silver foil were observed. Two representative areas of these fractures are reported in Figure 4. Fig. 4a shows an optical microscopy image of a fracture point (red arrow) in the left-central part of the sample as depicted in Figure 2. Starting from the bottom of the picture, a dark grey layer of siderite was observed underneath the silver foil (as described for Fig.3). At the location of the fracture, a thin filament (yellow arrow) of light grey corrosion products, identified as magnetite by µ-Raman measurements, appeared to protrude out of the silver foil, perpendicular to its surface. Other islets of white corrosion products, within a grey goethite matrix were observed on the external area, together with some porosities (black areas). Fig. 4b shows another area of the sample, at the right extremity of the object, where two fractures (red arrows) were recognizable on the silver foil. From the bigger fracture, a filament (yellow arrow) of light grey corrosion products identified as magnetite by µ-Raman measurements, was observed as well. The same light grey magnetite was observed underneath the silver foil in this area of the sample (peripheric area on the right extremity of the cross-section).

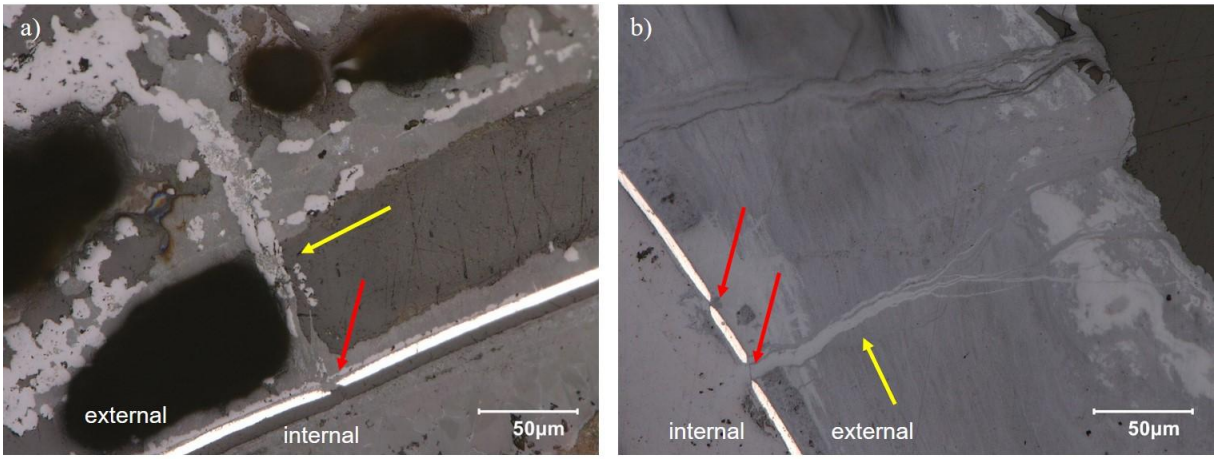

Figure 4 Optical microscopy images of different areas located in the ROI1as depicted in Figure 2, adjacent to the silver foil, in a) the central-left part, and b) the right part of the sample, showing fractures of the foil (red arrows), associated to specific morphologies of corrosion products on the external side perpendicular to the silver foil surface (yellow arrows).

On Figure 5 it was possible to observe another area of ROI1, on the left upper part of the cross-section. In Figure 5a, starting from the top, a grey area composed of the embedding resin followed an external thick layer (100-400 µm) of corrosion products, corresponding to the first stratum of goethite and magnetite/maghemite, as described in Figure 3. A discontinuity was observed in the middle of this marbled goethite/magnetite/maghemite layer. SEM-EDX identified the inclusion to be a homogeneous, Si-rich matrix (44 wt.% Si,47 wt.% O, 6 wt.% Ca, 2wt.% Al). These results suggested the presence of altered glass, which features a soda-lime silicate composition in good agreement with the composition of Roman glass found in the literature [30–32]. The absence of Na may be explained by glass alteration,

involving the process of interdiffusion between alkali ions from the glass and hydrated species from the environment, leading to the formation of a hydrated, porous and alkali-depleted altered glass [31,33–37]. The Raman spectra collected in this Si-rich matrix (exceptionally with a green laser power of 2.55 mW) are reported in Figures 5f and 5g for the low and high wavenumber regions, respectively. They showed an intense large peak at 380-490 cm^{-1}, a large weak peak at 780-830 cm^{-1}, as well as a large structure with two peaks at 955 and 990 cm^{-1}. These peaks correspond to the bending of the Si-O bonds, the vibrations of the monomeric isolated SiO_4 (Q^0, zero bridging oxygen), and the stretching of the Si-O bonds, allowing to attribute the spectrum to the presence of glass [38–42]. Moreover, the strong contribution of the Q^1 and Q^2 (one and two bridging oxygen respectively) bands around 950 cm^{-1} and the absence of bands corresponding to Q^3 and Q^4 species (around 1100 cm^{-1}) shows that the glass had a strongly depolymerized structure, congruous with altered glass [39,40,43,44]. Moreover, a broad and intense band was identified around 3400 cm^{-1}, attributed to the OH stretching vibrations of H_2O molecules and OH groups [45], in agreement with the altered glass hypothesis. An additional strong and sharp peak at 1076 cm^{-1} was identified in the Raman spectrum and could be attributed to the presence of micro/nano crystals of carbonates. This altered glass showed a network of fractures, filled with iron corrosion products (66 wt.% Fe and 31 wt.% O by SEM-EDX, previously identified as goethite).

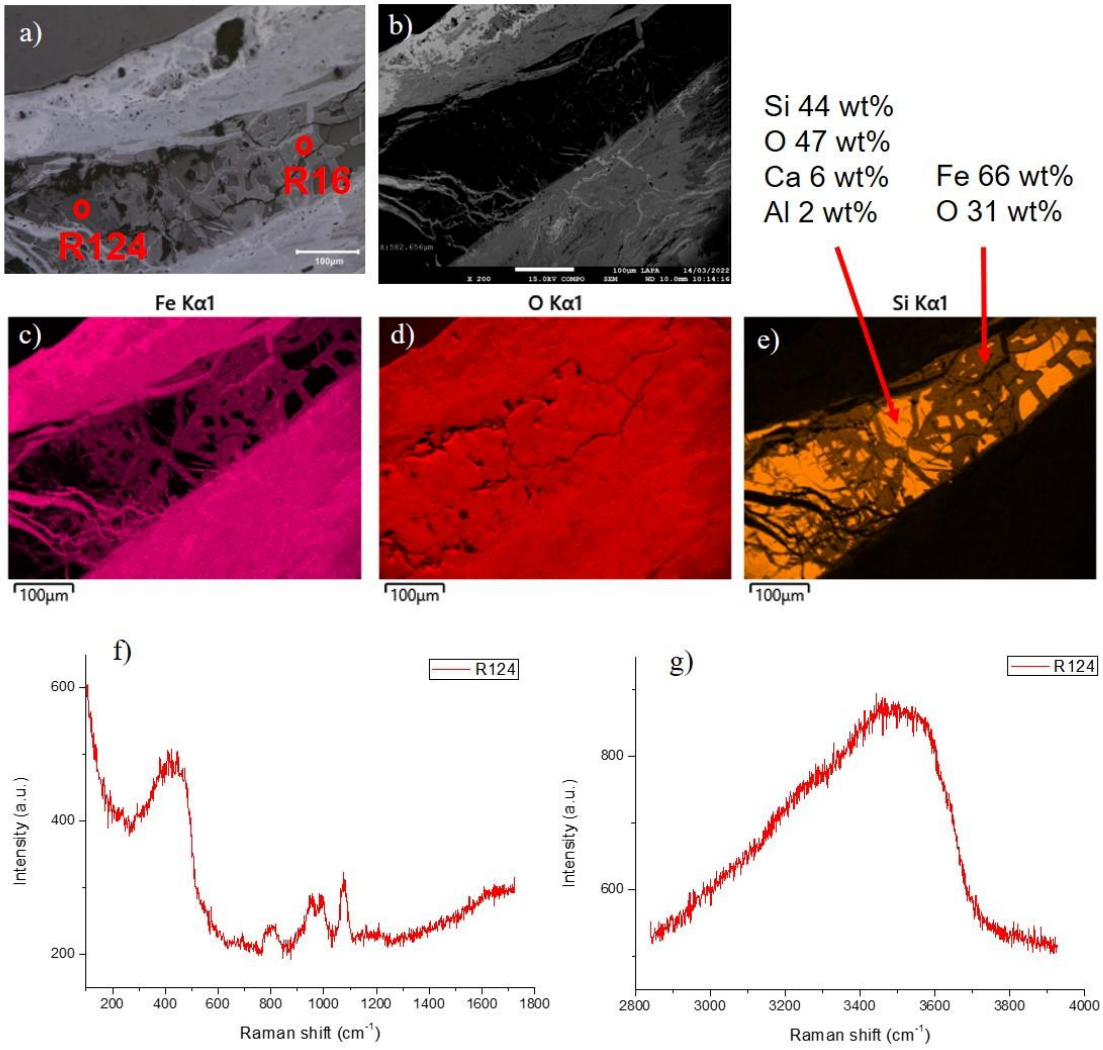

Figure 5 a) Optical microscopy image (with identification of the µ-Raman analysis point) of an area in the ROI1 in the upper part of the sample as depicted in Figure 2, b) backscattered electron image and EDX elemental mapping for c) Fe, d) O and e) Si with EDX composition of the different corrosion products. µ-Raman spectra obtained for R124 analysis point in f) the 100-1800 cm^{-1} region and g) the 2800-4000 cm^{-1} region.

3.2 Region of Interest 2: bottom area

As presented in Figure 6, the bottom of the sample showed alternating bands of grey, beige, and whitish local corrosion products (marbled corrosion structure). A detail area recorded in backscattered electron mode is showing the high brilliancy contrast between whitish and grey areas, with intermediate light grey bands corresponding to the beige ones in optical microscopy. The grey corrosion products had an EDX composition of 66 wt.% of Fe, 32 wt.% of O, and a Raman spectrum with peaks at 301, 388, 482, 550 and 685 cm^{-1} (point R70 in Fig. 6c), identified as goethite. The beige corrosion products contained 70 wt.% of Fe and 28 wt.% of O. Two different Raman spectra were recorded corresponding to either magnetite (peaks at 308, 542, 669 cm^{-1}, spectrum R73, Fig. 6e) or a mixture of maghemite/magnetite

(with a main broad band around 700 cm^{-1} and two shoulders at 660 and 720 cm^{-1}, as well as additional peaks at 380 and 510 cm^{-1}, spectrum R77, Fig. 6f). The whitish corrosion products consisted of 71 wt.% of Fe and 26 wt.% of O and featured a Raman spectrum with peaks at 228, 296, 415, 510, 672, 1333 cm^{-1} (R71, Fig. 6d) characteristic of hematite (α-Fe_2O_3). Similar spectra were recorded in the bottom left and right sides of the sample. Above this marbled structure, the void was filled with resin and less compact corrosion products, constituted mainly of magnetite and goethite.

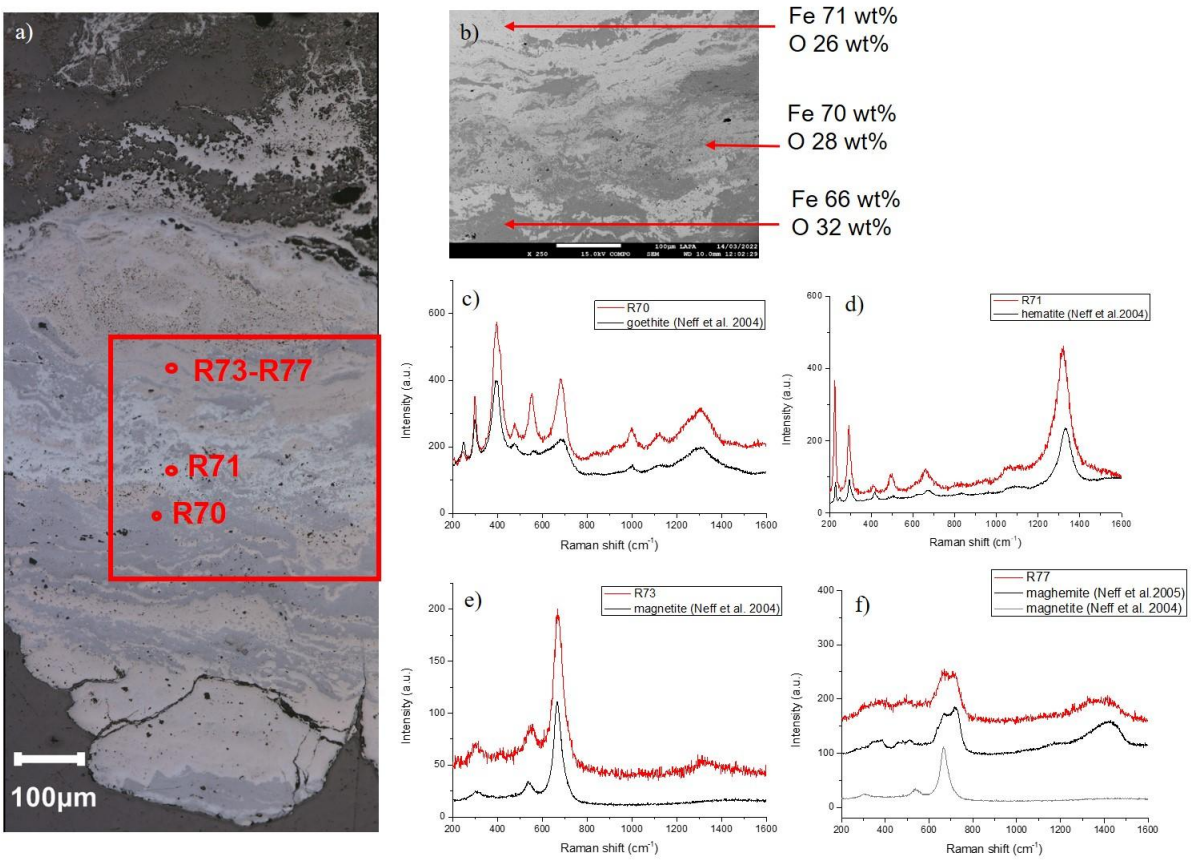

Figure 6 a) Optical microscopy image (with identification of the µ-Raman analysis points) of the ROI2 area on the bottom of the sample as depicted in Figure 2. b) Backscattered electron image with EDX composition of the different corrosion products and EDX and µ-Raman spectra for c) R70 analysis point, d) R71 analysis point, e) R73 analysis point, f) R77 analysis point.

3.3 Region of Interest 3: central area

The central part of the sample, within the cavity, where the corrosion products partially filled the cavity underneath the silver foil, predominantly contained spheroidal light grey nodules with varying shape and dimension. Two overviews of different areas of ROI3 are reported in Figure 7a and 7b, showing that these nodules had heterogeneous morphologies and distribution in the volume. They had mainly a spheroidal form with diameter around 50-100 µm, but some of them showed elongated shapes that could

reach up to 500-1000 µm in length. Some nodules were plain and dense, others showed heterogeneous features. Their characterization, reported in Figures 7 and 8, led to the identification of 2 main types of nodules with several intermediate typologies, that will be detailed in the following paragraphs. All the nodules were trapped in a dark grey matrix.

In Figure 7c several plain nodules appeared light grey in backscattered electron mode. Their Raman spectra featured peaks at 308, 542 and 669 cm^{-1} characteristics to that of magnetite (representative spectrum R01 in Fig. 7e) and from now on referred to as "Type I nodules". The matrix around the nodules showed peaks at 285, 729, 1084 cm^{-1} and was identified as siderite (representative spectrum R04, Fig. 7f). An intermediate elongated nodule with a heterogeneous central area was also visible in Fig. 7c. In Figure 7d, several nodules were observed, composed of a dark matrix in which were embedded numerous light grey micro-grains (1-10 µm). These micro-grains showed Raman peaks at 308, 542 and 669 cm^{-1} and were identified as magnetite (R125, Fig. 7e, obtained at low power intensity in order to avoid heat transformation because these micro-grains were more sensitive to this phenomenon). In addition, the dark matrix inside the nodule showed peaks at 301, 388, 482, 550 and 685 cm^{-1} and was identified as goethite (R122, Fig. 7g, obtained with a 785 nm laser in order to avoid a strong fluorescence phenomenon). These nodules having a goethite matrix with magnetite micro-nodules will be referred to as "Type II nodules".

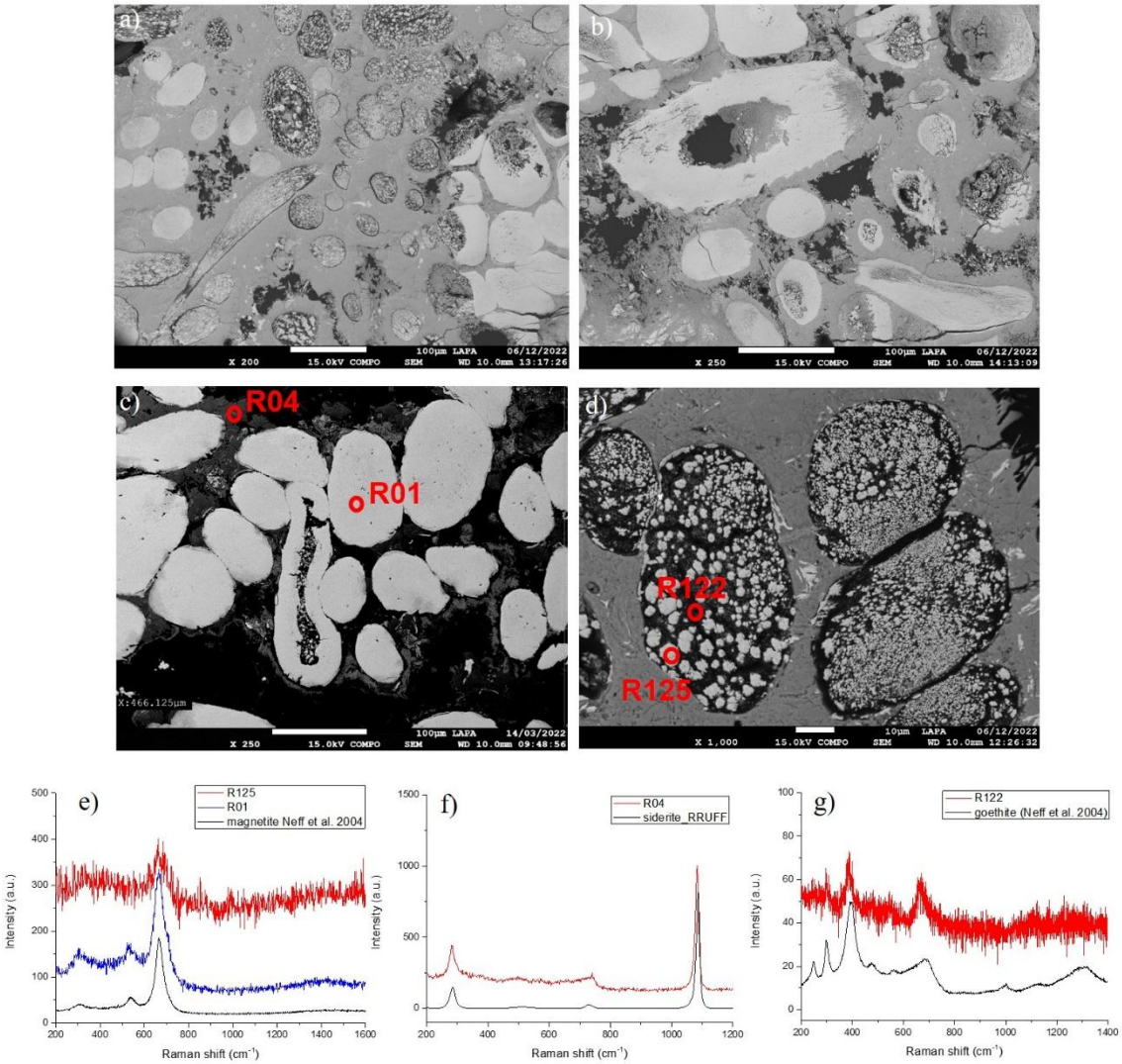

Figure 7 SEM backscattered electron images of a-b) different kinds of nodules distributed heterogeneously in the central area of the sample (ROI1), c) majority of Type I nodules with identification of μ-Raman analysis points, d) Type II nodules with identification of μ-Raman analysis points. Raman spectra for e) R01 and R125 analysis points, f) R04 analysis point, g) R122 analysis point.

Figure 8 depicts different morphologies of nodules (only SEM-SE images are reported, Raman spectra used to identify the corrosion products are not shown). In Figure 8a, different plain "Type I" magnetite nodules, both spheroidal and elongated and embedded in the siderite matrix, were observed in secondary electron mode. At the center of Fig. 8a, an elongated nodule had a low-density zone in the center, where it was possible to observe sub-micrometer grains with diameter of the order of 100 nm (Fig. 8b). In Figure 8c, it was possible to recognize on the left side a "Type II" nodule, constituted of small grains (1-5 μm diameter) made of magnetite inside a goethite matrix. On the right side of Fig. 8c, another nodule showed an intermediate morphology where half of it was a Type I morphology, while the other half was a Type II morphology. The interface between these two areas is detailed in Fig. 8d and showed

293 a disassembling of the micro-grains. A kind of intermediate nodule is reported in Fig. 8e, showing a
294 slightly deformed spherical morphology with an external magnetite border and an empty central area.
295 Fig. 8f shows a close-up of the granular, sub-micrometer interface between magnetite matrix and central
296 cavity.

297

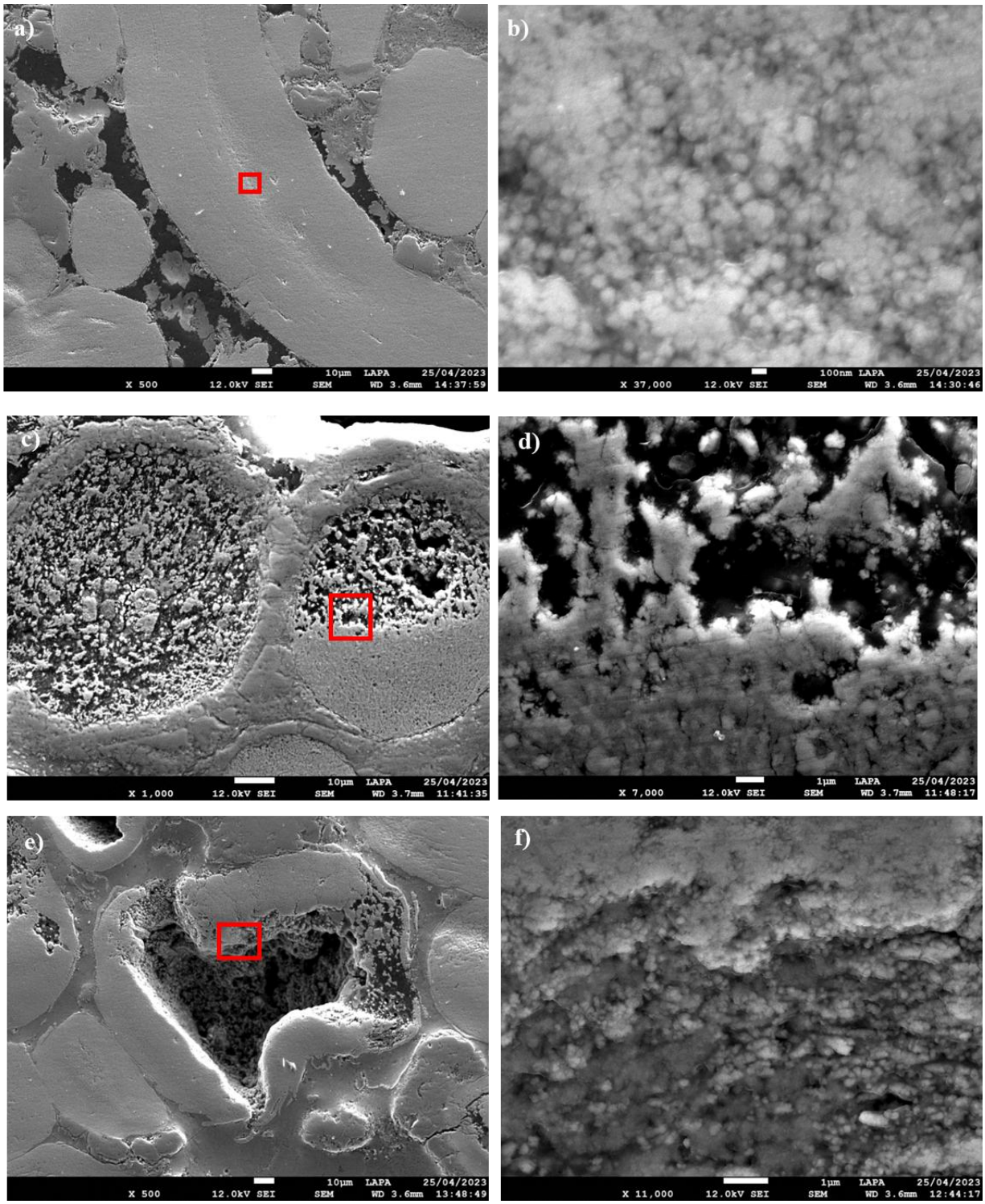

Figure 8 SEM secondary electron images of different morphologies of nodules. The red squares on the images on the left represent the areas where the detailed images on the right side are taken. a) Type I elongated nodule with a b) low-density area in the center. c) Type II nodule on the left, and an intermediate nodule on the right, with d) irregular interface. e) Intermediate nodule with empty f) central area.

In Figure 9, a summary of the results obtained with the different analytical techniques isreported as a color-coded schematic representation of the cross-section of the sample. The silver foil appeared mostly uncorroded, except for some areas of ROI1 where small S-rich crystals were observed adjacent to the silver foil, which might be interpreted as silver sulfides (blue in Figure 9), but it was not possible to confirm their presence by Raman spectroscopy. The different types of nodules identified are reported as well: a Type I nodule with a plain homogeneous structure composed of magnetite, a Type II nodule composed of a goethite matrix with scattered micrograins of magnetite. Then, three additional intermediate nodule types are reported: a type of nodule that is a mixture of Type I and Type II, showing a clear interface between the two areas, and a type of nodule having an external magnetite area and internal area that can be empty or filled with goethite or goethite and micrometric grains of magnetite.

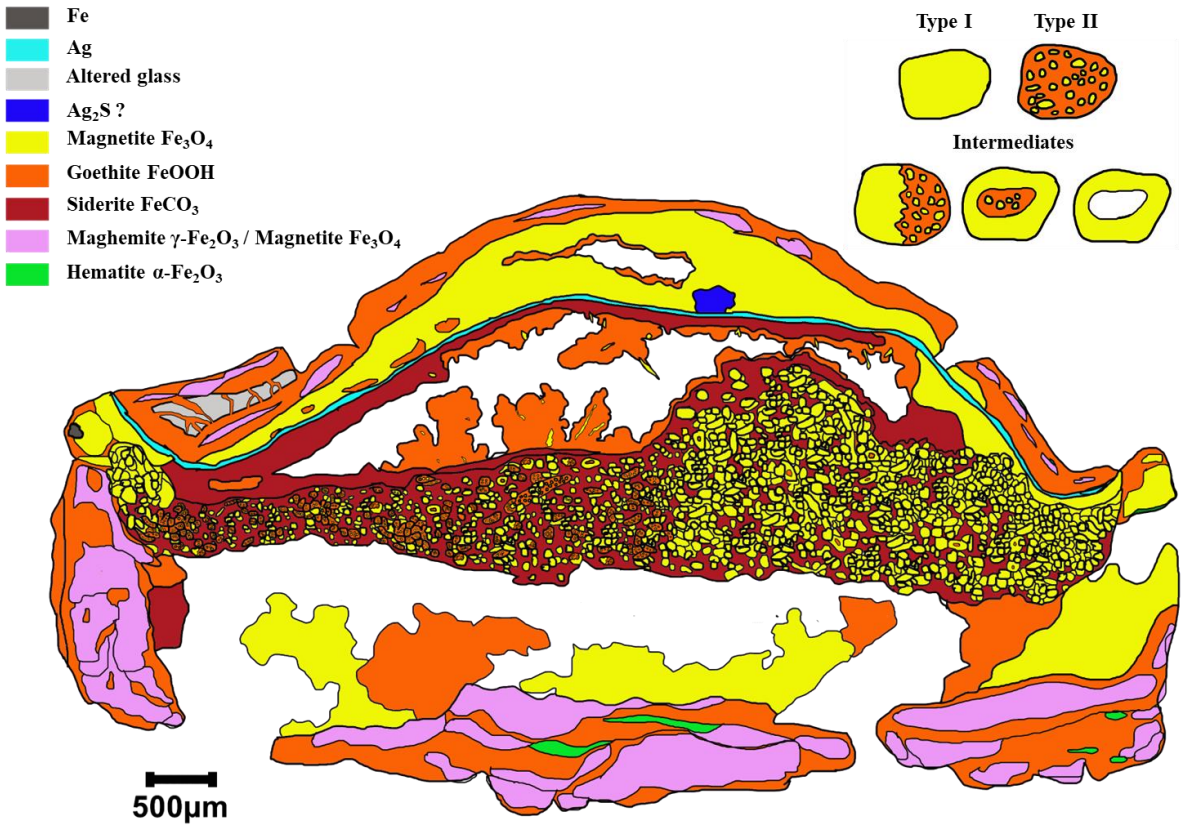

Figure 9 Schematic drawing of the cross-section of the sample with color-coded distribution of the identified metals and corrosion products. On the right-top, a schematic representation of the different kinds of nodular corrosion products identified in the center of the sample: Type I plain magnetite nodules, Type II nodules with magnetite micro-grains in a goethite matrix, and a series of intermediate heterogeneous nodules.

Discussion

4.1 Original state of the artefact

The characterization of the object described in this work allowed drawing additional conclusions regarding its original state, complementary to those based on the previous non-invasive characterization by Krieg et al.[4]. The presence of the silver foil was confirmed and its precise composition and thickness determined. Its low thickness (4-5 μm), associated to the presence of 2 wt% Cu and the absence of inclusions, denoted a well mastered silversmith ability [46]. Remnants of altered glass trapped in the iron corrosion products were discovered, thus validating the presence of a glass inlay on the surface of the bezel ring, not identified before, and contributing to reconstruct the history of the object. A schematic representation of the pristine object as it was during its usage (iron ring structure with silver foil and a glass inlay on the top) is depicted in Figure 1a. Thanks to the identification of the typology of the ring (Type 2a) by Krieg et al. [4], it is now possible to compare the original structure to the one observed on the corroded object. As a first observation, it is possible to notice that the bottom part of the ring loop was absent, and that almost no metallic iron was present, attesting the advanced stage of corrosion of the object. For this complex object, the classical generalized corrosion pattern described in the literature for archaeological objects [6,9], constituted of residual metal, original surface, dense product layer and transformed medium, was not observed. The residual iron metal was only present in a tiny area of a few μm^2 on the left of the observed cross-section (Figure 2 black arrow). The original surface was difficult to locate. The transformed medium was absent because it was completely removed by sand-blasting after the archaeological excavation. Instead, the corrosion system was constituted of different areas showing contrasting morphologies and composition.

4.2 Inferring on processes occurring while the ring was in the ground

The most striking feature observed on the corroded sample was the presence of dense, homogenous iron corrosion products without sediment components on top of the silver foil (and therefore interpreted as the original surface whilst cleaning by micro-sandblasting), where no metallic iron was present originally. Moreover, the silver foil and the adjacent corrosion products presented a deformed bulged shape where it was originally supposed to be flat, delimiting a cavity beneath, containing so far unobserved nodular corrosion products. Following the microchemical characterization results, it was possible to distinguish three macro-domains with unique chemical environments (ROI1, ROI2, and ROI3 as described in the Results section), giving rise to entirely different patterns of corrosion products on the exterior and within the cavity formed underneath the silver foil. Let us consider them separately.

4.2.1 Top area (outside of the silver foil)

The presence of the magnetite and the goethite/magnetite/maghemite external strata of corrosion products described in the ROI1 on top of the silver foil was definitely not linked to in-situ iron corrosion, because no metallic iron was originally present in this area of the ring. Their presence could thus be explained by a migration of iron ions coupled to a subsequent redeposition. It is possible to assume that, given the characteristics of the soil where the ring was found, subject to frequent groundwater

fluctuations on rainfall, most of the corrosion mechanisms happened in a water-rich, at least temporarily oxygenated environment. Thus, the iron corrosion processes happening beneath the silver foil, which will be discussed later in this paper, likely led to an enrichment of iron ions in solution (probably coupled to a pH drop, which favored their stability in solution [47]). This iron-rich solution plausibly passed through the silver foil barrier through the fracture points observed on it. It was not possible at this time, to identify the moment at which these deformation and cracking happened during the corrosion history of the object. The processes leading to the deformation of the silver foil will be investigated in a following work, based on experimental evidence. Once this iron-rich solution reached the external environment (the soil), it led to the precipitation of at first a thick magnetite layer (mixed Fe(II)/Fe(III) phase) adhering to the silver foil, followed by the precipitation of a mixture of hydroxides and oxides like goethite and maghemite (Fe(III) phases). This sequence was suggested by the fact that magnetite was located more internally than the pure Fe(III) phases. The relative position of these layers, showing an increasing oxidation state from the silver foil to the more external areas in contact with the soil, suggest a change in the environmental conditions from the one compatible with the precipitation of magnetite to the one, more aerated favoring the precipitation of pure Fe(III) phases.

4.2.2 Original main body of the ring

The bottom peripheral areas of the object described in ROI2 corresponded to the original main body of the iron ring, partially consumed during the corrosion process (the bottom part of the loop was absent). The corrosion products observed in this area were the result of in-situ metallic iron corrosion, characterized by direct dissolution and precipitation of corrosion products. The marbled structure described in ROI2 showed Fe(III)-bearing phases, mainly goethite and maghemite. A mechanism for its formation was proposed by Neff et al. [6]. Goethite was probably formed from amorphous precursors, including 2-line ferrihydrite (2l-$Fe(OH)_3$), as a result of a thermodynamic transformation towards a more stable phase. Iron oxyhydroxide formation and expansion likely caused the formation of small cracks parallel to the metal/corrosion products interface. These cracks may become saturated with water, while the corrosion front kept producing Fe(II) ions that could diffuse through the pores and cracks in the previously formed corrosion product layer, oxidize and precipitate in the fractures as magnetite or maghemite. This kind of marbled structure was generally attributed to corrosion phenomena in aerated environments [5,9,48], and was thus in agreement with an iron corrosion process happening in direct contact with the soil oxygenated environment. The localized presence of hematite in this marbled structure, which is an iron oxide not usually observed in archaeological objects [6,9,10,49], furthermore provided valuable insights into the predominant physico-chemical parameters at different locations of interest over time. The formation of hematite and goethite from primary, amorphous corrosion products like 2-line ferrihydrite are generally controlled by the temperature and pH of the electrolyte. In buffered electrolytes, the formation of goethite is favored at either acidic (pH < 4) or alkaline (pH > 10) conditions, whilst hematite either forms at elevated temperatures or circumneutral pH [50,51]. In

unbuffered electrolytes, i.e. conditions more representative of natural environments, hematite formation can be favored from mildly acidic (pH = 3-6) to mildly alkaline (pH = 9-10) pH [52]. The unprecedented occurrence of both phases in direct vicinity to one another and the preferential stabilization of hematite at low temperatures could be indicative of local pH variations. At moderate pH, the driving force for the redissolution of primary 2-line ferrihydrite is low. Phase transformation of hematite thus proceeds via an internal dehydration of ferrihydrite aggregates [53–55]. In contrast, the precipitation of goethite occurs from solution, via aqueously dissolved $Fe(OH)_2^+$ at acidic and $Fe(OH)_4^-$ at alkaline pH, respectively [50,51,56]. The transformation pathways from amorphous 2-line ferrihydrite to more crystalline corrosion products are schematically illustrated in Figure 10. As a consequence of these mechanistic differences, the conversion of 2-line ferrihydrite at neutral to mildly alkaline pH is concluded within days to months of equilibration time. At highly alkaline pH on the other hand, the increased driving force of dissolution and aqueous $Fe(OH)_4^-$ concentration causes the predominant stabilization of goethite after several hours [57]. An overview of the transformation rate of 2-line ferrihydrite as estimated by the decrease of its solid mol fraction over time is provided in Supplementary Information, Figure S1.

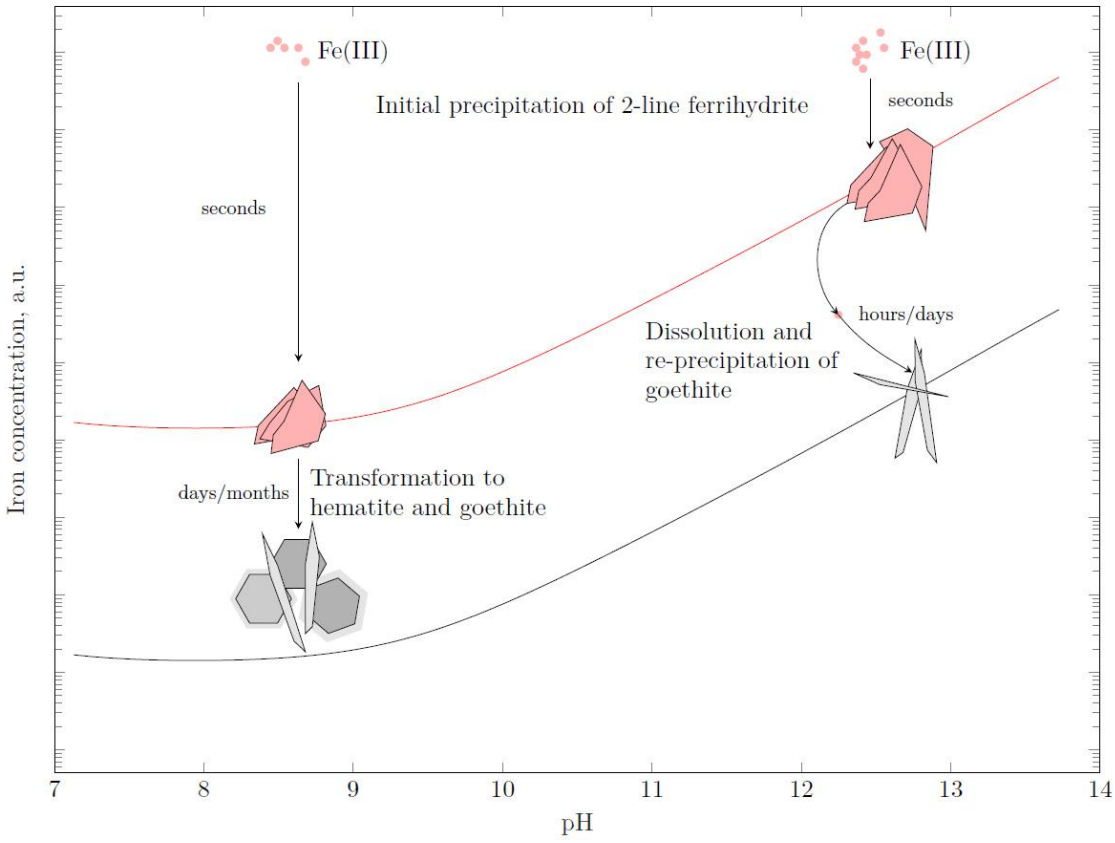

Figure 10 Schematic diagram of the precipitation of 2-line ferrihydrite (2l-$Fe(OH)_3$, pink in the figure) from aqueous Fe(III) species and its subsequent transformation to hematite and goethite (circumneutral pH) and goethite (alkaline pH).

4.2.3 Zone between silver foil and iron body

As stated in the results, the "inner" part of the artefact, described as ROI3, showed completely different features than the outer parts. Three characteristics were evidenced in the inner part: i) a plurimillimetric cavity, ii) the significant presence of siderite, and iii) the presence of nodular corrosion products embedded by this siderite. The spheroid or elliptic shape of the nodules suggested a nucleation/growth process from an iron-rich solution. Thanks to the fact that siderite embedded them (see Fig. 7), it can be reasonably argued that these nodules formed at an early stage of the corrosion process happening in an internal empty volume of the object, and that the siderite formed around them at a later step. At this point the question rises about the cavity in which both the nodules and the siderite are located. This cavity might be pre-existent or contemporary to the formation of the nodules, and its volume might also have evolved in a posterior step, after the formation of the nodules. The formation of this plurimillimetric cavity is most likely linked to the deformation of the silver foil. The study of the mechanism of this deformation process is beyond the scope of this work. However, based on the characterization results presented in this paper, it was possible to discuss and propose some hypotheses on the corrosion mechanisms happening at the interstice between the silver foil and the metallic iron (an interstice that will become a large cavity at a certain point indetermined in time).

As already stated, because of the finding of the object in an area subject to frequent flooding, it is possible to hypothesize that the object corrosion happened in a water-rich, at least temporarily oxygenated environment. Another consideration is the presence of two different metals, iron and silver, in contact with each other. This could favor galvanic corrosion processes, with the silver foil acting as a cathode and the iron ring as an anode [4]. Therefore, the anodic reaction (metallic iron oxidation) likely led to the release of Fe(II) ions in the solution trapped between the iron ring body and the silver foil. The stability of these iron ions in solution was enough to permit them to remain soluble and diffuse to the outside of the silver foil to form the ROI1 corrosion products previously discussed. This could be explained by a low local pH in the cavity possibly linked to Fe(II) hydrolysis. The dissolved Fe(II) partially oxidized and hydrolysed to form $Fe(OH)_3(aq)$, $Fe(OH)_2^+$ or $FeOH_2^+$, depending on the initial pH [28].

At a certain point during the corrosion process, local conditions within the cavity must have reached the ones compatible with the stability of magnetite, explaining the formation of Type I nodules. The continuous electrochemical formation of Fe(II) ions induced the supersaturation of the solution with respect to at least one of the Fe(II), mixed Fe(II)-Fe(III) and Fe(III) corrosion products observed. The formation of magnetite may have proceeded initially via (i) the Schikorr reaction from $Fe(OH)_2(s)$ precursors, through the co-precipitation of other iron (hydr)oxides including goethite and akaganéite [58,59] or (ii) from solution through agglomeration of nanometer-sized precursors [60,61]. As $Fe(OH)_2(s)$ has not been identified amongst the corrosion products formed, it follows that it either

transformed completely over time, or that the nucleation and growth process [60] was the main pathway of magnetite formation. The morphology of the nodules might recall the one of iron oxides found in natural sedimentary rocks formed under hydrothermal influence [62,63] whose formation is caused by periodic remobilization by water flows. Similar conditions in the environment of the buried ring might be attributed to the continuous fluctuation of the groundwater circulation in the soil of the archaeological site. It is essential to take these circumstances into account when assessing the nature and spatial distribution of the corrosion products characterized.

Type II nodules, consisting of a mixture of magnetite and goethite, can be attributed either to the direct co-precipitation of both phases at the beginning of the corrosion process already described, or to a later transformation of the Type I magnetite nodules. In this last case, the formation of the Type II nodules might be explained by a following step of dissolution/oxidation/reprecipitation. Over time, acidification of the electrolyte may have caused dissolution of the initial nodules as aqueous Fe(II) and Fe(III) complexes. Fe(II) complexes released may have oxidized further, (i) due to the remaining oxygen dissolved in the cavity, or (ii) via the reduction of water in anaerobic conditions [64], or (iii) by a renewal of oxygen in the solution caused by groundwater fluctuations. The resultant ferric hydrolysis products subsequently precipitated to form goethite from solution. The hypothesized transformation mechanism was further supported by thermodynamic modelling simulations (see Methods part for details) of the stability of magnetite in the presence of oxygen. Figure 11a displays the mol fraction of magnetite and goethite as a function of the amount of oxygen added to the system at circumneutral pH. It is evident that the formation of goethite is thermodynamically favorable in aerated conditions. At pH 8.0, phase transformation proceeds readily for ~ 0.17 M of dissolved oxygen added. This onset is shifted towards successively lower O_2(aq) at mildly acidic pH. Figure 11b shows a close-up SEM image of a mixed-nodule Type I / Type II highlighting an ongoing transformation process fixed in time. The concave dissolution front, running through the precipitate on the left-sidesite, could mark the transitional progress of magnetite dissolution followed by the formation of goethite grains in direct proximity to the parent magnetite precipitate. In this scenario, the “intermediate” nodules were the result of the same dissolution/oxidation/reprecipitation mechanism that led to the formation of the Type II nodules, at different time of the ongoing transformation and observed from different spatial perspectives. They differed from one another due to the alignment of the dissolution front and sample cross-section, since the process observed in 2D happened in 3D. For the precipitates, where the sample cross-section aligned parallel to the dissolution plane, magnetite grains appeared to be enclosed within a goethite matrix (see Figure 7c). The nodulesshowing an interface between Type I and Type II (see Figure 8c) likely transformed via the same mechanism, but with a dissolution front perpendicular to the sample cross-section. Shape and location of the dissolution front, both within the magnetite nodules and at the cavity scale also appeared to be a consequence of the local chemical environment. It is possible to observe in the sample cross-section schematically displayed in Figure 9, that the majority of Type II nodules were

located on the middle to left side of the cut. Both the right and left openings of the cavity appeared to be sealed off with Type I nodules. Towards the middle of the cross-section, the size and number of pure magnetite nodules diminished. This gradient suggests that mass transfer from the region surrounding the artefact likely mitigated the environmental changes happening at the center of the cavity.

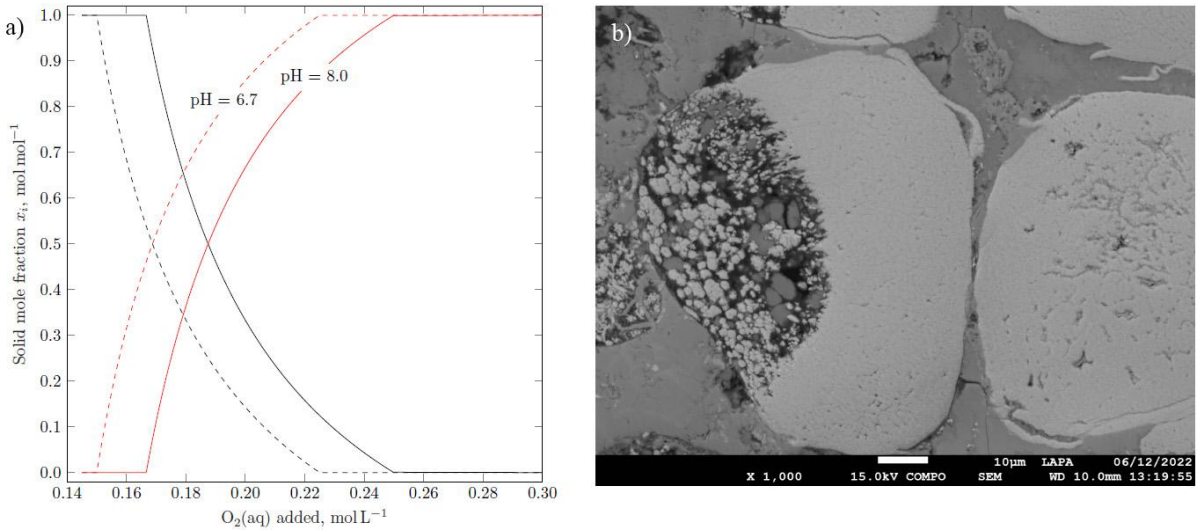

Figure 11 a) Mol fraction of α-Fe_3O_4(s) magnetite (black) and α-FeOOH(s) goethite (red) versus the total amount of O_2(aq) added at circumneutral pH, with b) a closeup SEM section of an intermediate nodule of magnetite that is partially converted to smaller goethite grains. Note that the x-axis represents the total amount of oxygen in the system.

The observation that siderite surrounded the nodules indicated that this phase appeared in a forthcoming stage of the process. Figure 12 displays the Pourbaix diagram of iron, containing iron oxides (Fe_3O_4(s), γ-Fe_2O_3), hydroxides (($Fe(OH)_2$(s)) and carbonate ($FeCO_3$(s)) phases, and their thermodynamic regions of stability as a function of the potential and the pH. At negative potentials and circumneutral pH, the formation of siderite is expected to compete with the formation of both magnetite and $Fe(OH)_2$(s). Magnetite on the other hand, a mixed Fe(II)/Fe(III) iron oxide, can further form directly via the oxidation of $Fe(OH)_2$, e.g. via the Schikorr reaction. In order to understand the competition between these phases and explain the abundance of siderite within the heterogeneous central area of the ring (see Figure 9), thermodynamic stability simulations were dissected into a pure Fe(II) system, considering the formation of $Fe(OH)_2$(s), and siderite. Figure 13 visualizes the competitive formation of siderite and $Fe(OH)_2$(s) within their overlapping regions of thermodynamic stability (Pourbaix diagram, Figure 12) as a function of the amount of H_2CO_3(aq) present in the system. This simulation confirmed that the siderite solid mol fraction is strongly dependent onthe amount of carbonates in solution and the pH, with its formation favored at lower pH values (Figs. 12-13).

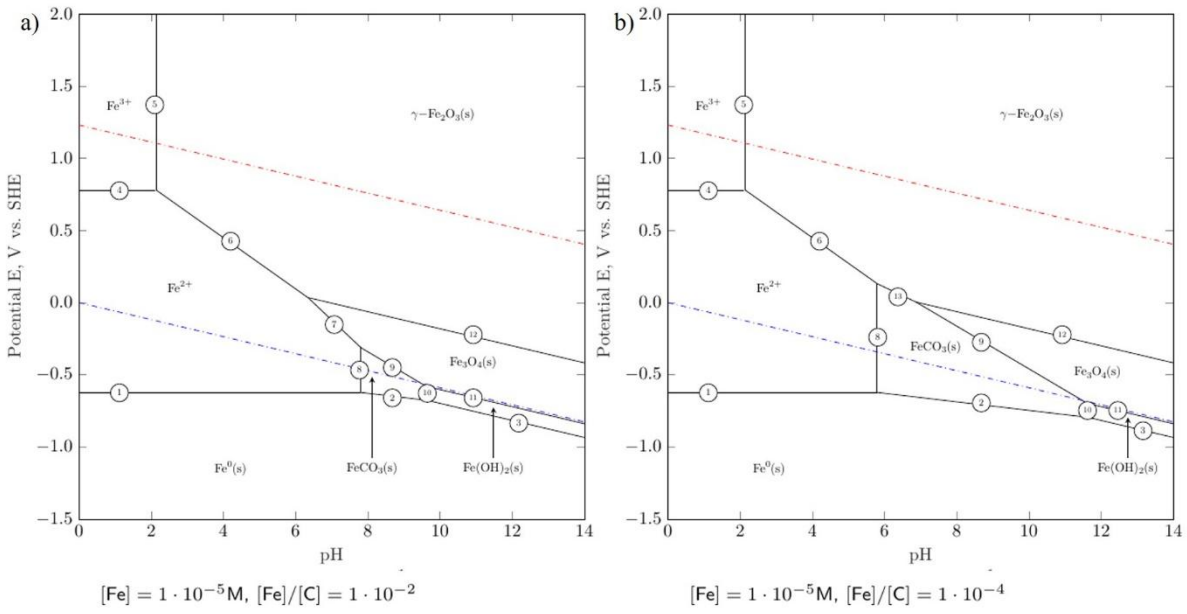

Figure 12 Pourbaix diagrams of iron containing selected aqueous iron complexes, (hydr)oxides and carbonate phases at an aqueous iron concentration of [Fe] = $1 \cdot 10^{-5}$ M and an aqueous carbonate concentration of a) [C] = $1 \cdot 10^{-3}$ M and b) [C] = $1 \cdot 10^{-1}$ M. Both diagrams were generated using the thermodynamic data published in Furcas et al.[28,56].

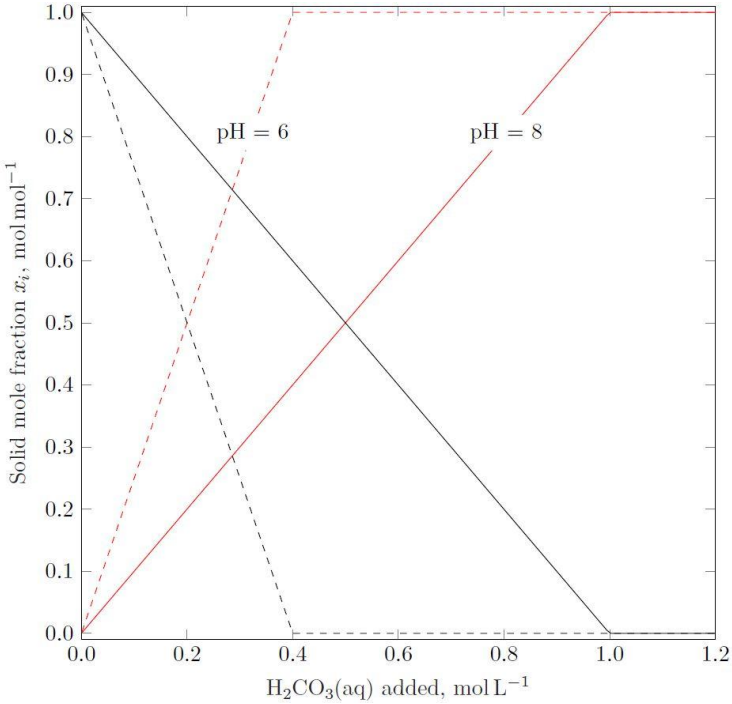

Figure 13 Mol fraction of $Fe(OH)_2$(s) (black) and $FeCO_3$(s) siderite (red) versus the total amount of H_2CO_3(aq) added at circumneutral pH. Note that the x-axis does not represent the aqueous concentration of H_2CO_3(aq) in equilibrium with both mineral phases but the total amount in the system.

From the Pourbaix diagram and from the $Fe(OH)_2/FeCO_3$ competition diagram, it can be recognized that the formation of siderite is favored by i) an increasing concentration of $H_2CO_3(aq)$, here coming from the burying environment of the object, ii) a decreasing pH, previously explained by iron hydrolysis causing a pH drop, and iii) a low oxygenation degree. It is also apparent that the amount of aqueously dissolved carbon to achieve full conversion had severe implications for the electrolyte buffering capacity and the partial anodic and cathodic half-cell reactions driving the transformation mechanism. The role of carbonates on iron corrosion mechanisms has been discussed in more detail elsewhere [65].

Noteworthy was the presence of a magnetite stratum replacing the siderite one in the external extremities of the cavity (for example, the area in Fig. 4b). This showed that, in the peripheral areas of the interstice, where the silver foil was more detached from the original iron surface, a partial communication with the external environment was possible, mitigating the pH drop in these peripheric areas, favoring the formation of magnetite over siderite.

In summary, successive variations in local internal conditions likely led to the formation of different thermodynamically stable phases inside the cavity. In the timeline of corrosion product formation, it appeared clear that the formation of magnetite nodules must have occurred before the stabilization of siderite. However, the exact chronological succession of the precipitation of goethite and siderite were difficult to reconstruct. For instance, it was not clear if the dissolution and reprecipitation process of magnetite nodules into goethite/magnetite nodules happened before or after the precipitation of siderite around them. An option was that firstly, both magnetite and mixed goethite/magnetite nodules formed, because of their higher thermodynamical stability than siderite in presence of oxygen. A second option was that the magnetite nodules formed first, then the siderite precipitated, caused by the change of conditions previously discussed, and only then, a later dissolution/reprecipitation step might have caused the transformation of nodules Type I to Type II and all the identified intermediates. The acidification of the solution within the cavity might indeed explain the redissolution process. In this scenario, the not observed dissolution of siderite might be explained by a strong concentration of carbonate ions in solution. Further research is needed to clarify certain mechanisms (deformation of the silver foil, competitive and time-dependent formation certain phases, etc.).

Conclusions

The Roman iron ring from Avenches exhibited a unique corrosion pattern, distinct from usual archaeological artifacts corroded in soils. The detailed characterization of the object described in this work allowed drawing additional conclusions regarding its original state. Traces of glass have been identified, which provided additional support to the earlier, tentative classification of this artefact as "Type 2a bezel ring". This classification means that the ring must have been flat initially, with glass on the silver foil. This, together with the observed bulging of the silver foil, thus suggested that the silver

552 foil deformed over the past two millennia. Microscale characterization of corrosion products identified
553 three macro-domains with distinct chemical environments:

554 1) On the external side, on top of the silver foil, a magnetite and a goethite/magnetite/maghemite
555 external strata were observed. Since these phases were precipitated distant from the original source of
556 metallic iron, the main body of the ring, it is inferred that transport of aqueous iron species to these outer
557 zones must have occurred, followed by precipitation of corrosion products.

558 2) In contrast, the bottom peripheral areas, corresponding to the original main body, were
559 characteristic of in-situ iron corrosion. The marbled structure observed here featured Fe(III)-bearing
560 phases like goethite and maghemite, which has been observed previously in similar artefacts.

561 3) The third zone, however, which is the cavity between the silver foil and the original iron body
562 of the ring, presented features so far unobserved in archaeological artefacts, namely nodular corrosion
563 products embedded in a siderite matrix. The most likely sequence of formation of these phases
564 (magnetite, goethite, then siderite) was reconstructed, but the duration of each of these steps remained
565 elusive.

566 This study provided insights into the unique corrosion pattern of the Roman ring from Avenches.
567 Analysis of the phases found in combination with theoretical thermodynamic considerations allowed to
568 infer the prevailing corrosion conditions and the properties of the aqueous electrolyte, offering a basis
569 for future studies on the physico-chemical processes influencing the deformation and deterioration of
570 this archeological ring over time.

571 Description of such corrosion systems lacks in the existing literature on archaeological artefacts and
572 their understanding will be valuable for a better interpretation of the artefacts history. Despite the
573 uniqueness of the corrosion morphology of this object which does not allow to extrapolate general
574 conclusions, this work represents another step towards a more general understanding of the corrosion
575 mechanisms of complex long-term systems and it will hopefully support the identification and
576 recognition of such a peculiar phenomenon on other objects in the future.

577 It also has to be stressed that crucial information, such as the presence of siderite and the one of
578 micrometric nodules of magnetite, was only detectable by the invasive characterization performed in
579 this study. This underlines the fact that, unfortunately, non-invasive approaches, despite delivering first
580 important information are in certain cases not sufficient to decipher the complex corrosion mechanisms
581 that potentially take place on an archaeological artefact. Only the invasive approach allowing one to
582 perform physicochemical and structural analytical methods at the micro scale is able to give this
583 information. Of course, that kind of approach cannot be systematically performed on heritage artefacts
584 and the studied ones must be carefully selected by archaeologists, restorers, conservators, conservation

scientists and corrosionists. Such study provides a typical example of a specific corrosion process, that could be in a second step extrapolated to other artifacts, only studied by non-invasive approaches.

Acknowledgments

The MetalPAT project was supported by the European cross-border cooperation programme Interreg V France-Switzerland 2014-2020 to which the authors would like to express their sincere thanks. It has received a grant of €186 599 from the European Regional Development Fund (ERDF) and additional funding from the cantons of Berne, Jura, Neuchâtel, Valais and Vaud (€90,830).

The authors from ETH Zurich are grateful to the European Research Council (ERC) for the financial support provided under the European Union's Horizon 2020 research and innovation program (grant agreement no. 848794).

Authors contributions

Valentina Valbi: Investigation, Visualization, Writing – Original Draft, Project administration. **Fabio Enrico Furcas:** Software, Formal analysis, Visualization. **Delphine Neff**: Supervision, Conceptualization. **Philippe Dillmann**: Supervision, Conceptualization, Funding acquisition. **Ueli Angst**: Supervision, Conceptualization, Funding acquisition. **Myriam Krieg:** Conceptualization, Resources. **Anika Duvauchelle:** Conceptualization, Resources. **Marion Berranger**: Resources. **Stefano Mischler:** Conceptualization. **Laura Brambilla**: Conceptualization. **Naima Gutknecht**: Resources. **Christian Degrigny:** Supervision, Conceptualization, Funding acquisition. **All the authors** contributed to Writing – Review & Editing.

Data Availability

All thermodynamic parameters are provided in Supporting Information. The raw/processed analytical data are available on request from the corresponding author.

References

[1] P. Dillmann, European Federation of Corrosion, eds., Corrosion of metallic heritage artefacts: investigation, conservation and prediction of long term behaviour ; [based on papers presented at Eurocorr 2004 during the Corrosion of Heritage Artefacts Workshop and the common session with the 2nd Workshop on Prediction of Long Term Corrosion Behaviour in Nuclear Waste Systems], Woodhead Publ, Cambridge, 2007.

[2] P. Dillmann, D. Watkinson, E. Angelini, A. Adriaens, Corrosion and conservation of cultural heritage metallic artefacts, Woodhead Publishing Limited, 2013. https://doi.org/10.1533/9781782421573.

[3] C. Degrigny, P. Dillmann, C. Gaspoz, D. Neff, Exploitation and dissemination of MiCorr as a diagnostic support tool for heritage metals, in: Diagn. Conserv. 360°, Murray A., Vila A., 2022: pp. 357–369.
[4] M. Krieg, A. Duvauchelle, F. Furcas, U. Angst, M. Binggeli, Etude et analyses des processus de corrosion d'une bague en fer à paillon en argent d'Avenches / Sur Fouches, Bull. Assoc. Aventico 61 (2020) 35–66.
[5] D. Neff, S. Reguer, L. Bellot-Gurlet, P. Dillmann, R. Bertholon, Structural characterization of corrosion products on archaeological iron: an integrated analytical approach to establish corrosion forms, J. Raman Spectrosc. 35 (2004) 739–745. https://doi.org/10.1002/jrs.1130.
[6] D. Neff, P. Dillmann, L. Bellot-Gurlet, G. Beranger, Corrosion of iron archaeological artefacts in soil: characterisation of the corrosion system, Corros. Sci. 47 (2005) 515–535. https://doi.org/10.1016/j.corsci.2004.05.029.
[7] L. Bellot-Gurlet, D. Neff, S. Réguer, J. Monnier, M. Saheb, P. Dillmann, Raman Studies of Corrosion Layers Formed on Archaeological Irons in Various Media, J. Nano Res. 8 (2009) 147–156. https://doi.org/10.4028/www.scientific.net/JNanoR.8.147.
[8] M.C. Bernard, S. Joiret, Understanding corrosion of ancient metals for the conservation of cultural heritage, Electrochimica Acta 54 (2009) 5199–5205. https://doi.org/10.1016/j.electacta.2009.01.036.
[9] A.-L. Grevey, V. Vignal, H. Krawiec, P. Ozga, K. Peche-Quilichini, A. Rivalan, F. Mazière, Microstructure and long-term corrosion of archaeological iron alloy artefacts, Herit. Sci. 8 (2020) 57. https://doi.org/10.1186/s40494-020-00398-9.
[10] M. Bernabale, F. Cognigni, L. Nigro, M. Rossi, T. de Caro, C. De Vito, A comprehensive strategy for exploring corrosion in iron-based artefacts through advanced Multiscale X-ray Microscopy, Sci. Rep. 12 (2022) 6125. https://doi.org/10.1038/s41598-022-10151-w.
[11] W. Gerwin, R. Baumhauer, Effect of soil parameters on the corrosion of archaeological metal finds, Geoderma 96 (2000) 63–80. https://doi.org/10.1016/S0016-7061(00)00004-5.
[12] O. Oudbashi, A methodological approach to estimate soil corrosivity for archaeological copper alloy artefacts, Herit. Sci. 6 (2018) 2. https://doi.org/10.1186/s40494-018-0167-4.
[13] H. Matthiesen, L.R. Hilbert, D.J. Gregory, Siderite as a Corrosion Product on Archaeological Iron from a Waterlogged Environment., Stud. Conserv. 48 (2003) 183–194.
[14] Neff, P. Dillmann, M. Descostes, G. Beranger, Corrosion of iron archaeological artefacts in soil: Estimation of the average corrosion rates involving analytical techniques and thermodynamic calculations, Corros. Sci. 48 (2006) 2947–2970. https://doi.org/10.1016/j.corsci.2005.11.013.
[15] M. Saheb, D. Neff, Ph. Dillmann, H. Matthiesen, E. Foy, Long-term corrosion behaviour of low-carbon steel in anoxic environment: Characterisation of archaeological artefacts, J. Nucl. Mater. 379 (2008) 118–123. https://doi.org/10.1016/j.jnucmat.2008.06.019.
[16] M. Saheb, M. Descostes, D. Neff, H. Matthiesen, A. Michelin, P. Dillmann, Iron corrosion in an anoxic soil: Comparison between thermodynamic modelling and ferrous archaeological artefacts characterised along with the local in situ geochemical conditions, Appl. Geochem. 25 (2010) 1937–1948. https://doi.org/10.1016/j.apgeochem.2010.10.010.
[17] M. Saheb, J.-P. Gallien, M. Descostes, L. Raimbault, A. Perez, D. Neff, F. Marsal, D. Pellegrini, P. Dillmann, Influence of an aerated/anoxic transient phase on the long-term corrosion of iron, Corros. Sci. 86 (2014) 71–80. https://doi.org/10.1016/j.corsci.2014.04.040.
[18] S. Réguer, D. Neff, L. Bellot-Gurlet, P. Dillmann, Deterioration of iron archaeological artefacts: micro-Raman investigation on Cl-containing corrosion products, J. Raman Spectrosc. 38 (2007) 389–397. https://doi.org/10.1002/jrs.1659.
[19] C. Rémazeilles, M. Saheb, D. Neff, E. Guilminot, K. Tran, J.-A. Bourdoiseau, R. Sabot, M. Jeannin, H. Matthiesen, P. Dillmann, P. Refait, Microbiologically influenced corrosion of archaeological artefacts: characterisation of iron(II) sulfides by Raman spectroscopy, J. Raman Spectrosc. 41 (2010) 1425–1433. https://doi.org/10.1002/jrs.2717.
[20] S. Grousset, M. Bayle, A. Dauzeres, D. Crusset, V. Deydier, Y. Linard, P. Dillmann, F. Mercier-Bion, D. Neff, Study of iron sulphides in long-term iron corrosion processes: Characterisations of

archaeological artefacts, Corros. Sci. 112 (2016) 264–275. https://doi.org/10.1016/j.corsci.2016.07.022.
[21] R. Bertholon, Characterisation and Location of Original Surface of Corroded Metallic Archaeological Objects, Surf. Eng. 17 (2001) 241–245. https://doi.org/10.1179/026708401101517863.
[22] H. Guiraud, Bagues et anneaux à l'époque romaine en Gaule, Gallia 46 (1989) 173–211. https://doi.org/10.3406/galia.1989.2895.
[23] B. Lafuente, R.T. Downs, H. Yang, N. Stone, The power of databases: the RRUFF project., in: Highlights Mineral. Crystallogr., T Armbruster and R M Danisi, Berlin, Germany, 2015: pp. 1–30.
[24] D.A. Kulik, T. Wagner, S.V. Dmytrieva, G. Kosakowski, F.F. Hingerl, K.V. Chudnenko, U.R. Berner, GEM-Selektor geochemical modeling package: revised algorithm and GEMS3K numerical kernel for coupled simulation codes, Comput. Geosci. (2012). https://doi.org/10.1007/s10596-012-9310-6.
[25] T. Wagner, D.A. Kulik, F.F. Hingerl, S.V. Dmytrieva, GEM-SELEKTOR GEOCHEMICAL MODELING PACKAGE: TSolMod LIBRARY AND DATA INTERFACE FOR MULTICOMPONENT PHASE MODELS, Can. Mineral. 50 (2012) 1173–1195. https://doi.org/10.3749/canmin.50.5.1173.
[26] H.C. Helgeson, D.H. Kirkham, G.C. Flowers, Theoretical prediction of the thermodynamic behavior of aqueous electrolytes by high pressures and temperatures; IV, Calculation of activity coefficients, osmotic coefficients, and apparent molal and standard and relative partial molal properties to 600 degrees C and 5kb, Am. J. Sci. 281 (1981) 1249–1516. https://doi.org/10.2475/ajs.281.10.1249.
[27] P. Brown, C. Ekberg, Hydrolysis of metal ions, Wiley-VCH, Verlag GmbH & Co. KGaA, Weinheim, Germany, 2016.
[28] F.E. Furcas, B. Lothenbach, O.B. Isgor, S. Mundra, Z. Zhang, U.M. Angst, Solubility and speciation of iron in cementitious systems, Cem. Concr. Res. 151 (2022) 106620. https://doi.org/10.1016/j.cemconres.2021.106620.
[29] I. Grenthe, H. Wanner, I. Forest, OECD Nuclear Energy Agency, eds., Chemical thermodynamics of uranium, North-Holland ; Distributors for the U.S. and Canada, Elsevier Science Pub. Co, Amsterdam ; New York : New York, N.Y., U.S.A, 1992.
[30] A. Shortland, L. Schachner, I. Freestone, M. Tite, Natron as a flux in the early vitreous materials industry: sources,beginnings and reasons for decline, J. Archaeol. Sci. 33 (2006) 521–530.
[31] M. Verità, Modern and ancient glass : nature, composition and deterioration mechanisms, Mater. Cult. Herit. Their Environ. (2006).
[32] B. Gratuze, N. Schibille, I. Pactat, Glass in the Middle East and Western Europe at the End of the First Millennium CE, Transition from Natron to Plant Ash Soda or Forest Glasses, in: A.K. Kanungo, L. Dussubieux (Eds.), Anc. Glass South Asia, Springer Singapore, Singapore, 2021: pp. 21–38. https://doi.org/10.1007/978-981-16-3656-1_2.
[33] R.H. Doremus, Interdiffusion of hydrogen and alkali ions in a glass surface, J. Non-Cryst. Solids 19 (1975) 137–144. https://doi.org/10.1016/0022-3093(75)90079-4.
[34] A. Verney-Carron, S. Gin, G. Libourel, A fractured roman glass block altered for 1800 years in seawater: Analogy with nuclear waste glass in a deep geological repository, Geochim. Cosmochim. Acta 72 (2008) 5372–5385. https://doi.org/10.1016/j.gca.2008.08.018.
[35] A. Verney-Carron, S. Gin, P. Frugier, G. Libourel, Long-term modeling of alteration-transport coupling: Application to a fractured Roman glass, Geochim. Cosmochim. Acta 74 (2010) 2291–2315. https://doi.org/10.1016/j.gca.2010.01.001.
[36] S. Gin, L. Neill, M. Fournier, P. Frugier, T. Ducasse, M. Tribet, A. Abdelouas, B. Parruzot, J. Neeway, N. Wall, The controversial role of inter-diffusion in glass alteration, Chem. Geol. 440 (2016) 115–123. https://doi.org/10.1016/j.chemgeo.2016.07.014.
[37] S. Gin, J.-M. Delaye, F. Angeli, S. Schuller, Aqueous alteration of silicate glass: state of knowledge and perspectives, Npj Mater. Degrad. 5 (2021) 42. https://doi.org/10.1038/s41529-021-00190-5.

[38] D.W. Matson, S.K. Sharma, J.A. Philpotts, The structure of high-silica alkali-silicate glasses. A Raman spectroscopic investigation, J. Non-Cryst. Solids 58 (1983) 323–352. https://doi.org/10.1016/0022-3093(83)90032-7.
[39] P. Colomban, Polymerization degree and Raman identification of ancient glasses used for jewelry, ceramic enamels and mosaics, J. Non-Cryst. Solids 323 (2003) 180–187. https://doi.org/10.1016/S0022-3093(03)00303-X.
[40] P. Colomban, M.P. Etcheverry, M. Asquier, M. Bounichou, A. Tournié, Raman identification of ancient stained glasses and their degree of deterioration, J. Raman Spectrosc. 37 (2006) 614–626. https://doi.org/10.1002/jrs.1495.
[41] L. Robinet, C. Coupry, K. Eremin, C. Hall, The use of Raman spectrometry to predict the stability of historic glasses, J. Raman Spectrosc. 37 (2006) 789–797. https://doi.org/10.1002/jrs.1540.
[42] N. Trcera, S. Rossano, M. Tarrida, Structural study of Mg-bearing sodosilicate glasses by Raman spectroscopy, J. Raman Spectrosc. 42 (2011) 765–772. https://doi.org/10.1002/jrs.2763.
[43] A. Tournié, P. Ricciardi, P. Colomban, Glass corrosion mechanisms: A multiscale analysis, Solid State Ion. 179 (2008) 2142–2154. https://doi.org/10.1016/j.ssi.2008.07.019.
[44] F. Alloteau, O. Majérus, V. Valbi, I. Biron, P. Lehuédé, D. Caurant, T. Charpentier, A. Seyeux, Evidence for different behaviors of atmospheric glass alteration as a function of glass composition, Npj Mater. Degrad. 4 (2020) 36. https://doi.org/10.1038/s41529-020-00138-1.
[45] C. Le Losq, D.R. Neuville, R. Moretti, J. Roux, Determination of water content in silicate glasses using Raman spectrometry: Implications for the study of explosive volcanism, Am. Mineral. 97 (2012) 779–790. https://doi.org/10.2138/am.2012.3831.
[46] U. Zwicker, A. Oddy, S.L. Niece, Roman techniques of manufacturing silver-plated coins, in: Met. Plat. Patination, Elsevier, 1993: pp. 223–246. https://doi.org/10.1016/B978-0-7506-1611-9.50024-8.
[47] R.J. Lemire, U.R. Berner, C. Musikas, D.A. Palmer, P. Taylor, O. Tochiyama, J. Perrone, Chemical Thermodynamics of Iron, Part 1 - Chemical Thermodynamics, Nuclear Energy Agency of the OECD (NEA), 2013.
[48] A. Demoulin, C. Trigance, D. Neff, E. Foy, P. Dillmann, V. L'Hostis, The evolution of the corrosion of iron in hydraulic binders analysed from 46- and 260-year-old buildings, Corros. Sci. 52 (2010) 3168–3179. https://doi.org/10.1016/j.corsci.2010.05.019.
[49] I. Azoulay, E. Conforto, P. Refait, C. Rémazeilles, Study of ferrous corrosion products on iron archaeological objects by electron backscattered diffraction (EBSD), Appl. Phys. A 110 (2013) 379–388. https://doi.org/10.1007/s00339-012-7174-1.
[50] U. Schwertmann, J. Friedl, H. Stanjek, From Fe(III) Ions to Ferrihydrite and then to Hematite, J. Colloid Interface Sci. 209 (1999) 215–223. https://doi.org/10.1006/jcis.1998.5899.
[51] U. Schwertmann, H. Stanjek, H.-H. Becher, Long-term *in vitro* transformation of 2-line ferrihydrite to goethite/hematite at 4, 10, 15 and 25°C, Clay Miner. 39 (2004) 433–438. https://doi.org/10.1180/0009855043940145.
[52] S.A. Chen, P.J. Heaney, J.E. Post, P.J. Eng, J.E. Stubbs, Hematite-goethite ratios at pH 2–13 and 25–170 °C: A time-resolved synchrotron X-ray diffraction study, Chem. Geol. 606 (2022) 120995. https://doi.org/10.1016/j.chemgeo.2022.120995.
[53] W.R. Fischer, The Formation of Hematite from Amorphous Iron(III)Hydroxide, Clays Clay Miner. 23 (1975) 33–37. https://doi.org/10.1346/CCMN.1975.0230105.
[54] U. Schwertmann, Effect of pH on the Formation of Goethite and Hematite from Ferrihydrite, Clays Clay Miner. 31 (1983) 277–284. https://doi.org/10.1346/CCMN.1983.0310405.
[55] J.A. Soltis, J.M. Feinberg, B. Gilbert, R.L. Penn, Phase Transformation and Particle-Mediated Growth in the Formation of Hematite from 2-Line Ferrihydrite, Cryst. Growth Des. 16 (2016) 922–932. https://doi.org/10.1021/acs.cgd.5b01471.
[56] F.E. Furcas, B. Lothenbach, S. Mundra, C. Borca, C.C. Albert, O.B. Isgor, T. Huthwelker, U.M. Angst, Transformation of 2-line ferrihydrite to goethite at alkaline pH, (2023). https://doi.org/10.48550/ARXIV.2307.03267.

[57] F.E. Furcas, S. Mundra, B. Lothenbach, U. Angst, Speciation controls the kinetics of iron hydroxide precipitation and transformation, (2023). https://doi.org/10.48550/ARXIV.2311.12464.
[58] U. Schwertmann, R.M. Taylor, Iron Oxides, in: J.B. Dixon, S.B. Weed (Eds.), SSSA Book Ser., Soil Science Society of America, Madison, WI, USA, 1989: pp. 379–438. https://doi.org/10.2136/sssabookser1.2ed.c8.
[59] T. Ahn, J.H. Kim, H.-M. Yang, J.W. Lee, J.-D. Kim, Formation Pathways of Magnetite Nanoparticles by Coprecipitation Method, J. Phys. Chem. C 116 (2012) 6069–6076. https://doi.org/10.1021/jp211843g.
[60] J. Baumgartner, A. Dey, P.H.H. Bomans, C. Le Coadou, P. Fratzl, N.A.J.M. Sommerdijk, D. Faivre, Nucleation and growth of magnetite from solution, Nat. Mater. 12 (2013) 310–314. https://doi.org/10.1038/nmat3558.
[61] J. Baumgartner, R.K. Ramamoorthy, A.P. Freitas, M.-A. Neouze, M. Bennet, D. Faivre, D. Carriere, Self-Confined Nucleation of Iron Oxide Nanoparticles in a Nanostructured Amorphous Precursor, Nano Lett. 20 (2020) 5001–5007. https://doi.org/10.1021/acs.nanolett.0c01125.
[62] M. Di Bella, G. Sabatino, S. Quartieri, A. Ferretti, B. Cavalazzi, R. Barbieri, F. Foucher, F. Messori, F. Italiano, Modern Iron Ooids of Hydrothermal Origin as a Proxy for Ancient Deposits, Sci. Rep. 9 (2019) 7107. https://doi.org/10.1038/s41598-019-43181-y.
[63] M. Rudmin, S. Banerjee, P. Maximov, A. Novoselov, Y. Trubin, P. Smirnov, A. Abersteiner, D. Tang, A. Mazurov, Origin of ooids, peloids and micro-oncoids of marine ironstone deposits in Western Siberia (Russia), J. Asian Earth Sci. 237 (2022) 105361. https://doi.org/10.1016/j.jseaes.2022.105361.
[64] S. Mundra, J. Tits, E. Wieland, U.M. Angst, Aerobic and anaerobic oxidation of ferrous ions in near-neutral solutions, Chemosphere 335 (2023) 138955. https://doi.org/10.1016/j.chemosphere.2023.138955.
[65] F. Martinelli-Orlando, W. Shi, U. Angst, Corrosion Behavior of Carbon Steel in Alkaline, Deaerated Solutions: Influence of Carbonate Ions, J. Electrochem. Soc. 167 (2020) 061503. https://doi.org/10.1149/1945-7111/ab7d44.

801